

Manipulation of topological phase transitions and the mechanism of magnetic interactions in Eu-based Zintl-phase materials

Bo-Xuan Li,^{1,2} Ziyin Song,^{1,2} Zhong Fang,^{1,2} Zhijun Wang,^{1,2} and Hongming Weng^{1,2,3,*}

¹Beijing National Laboratory for Condensed Matter Physics and Institute of Physics, Chinese Academy of Sciences, Beijing 100190, China

²University of Chinese Academy of Sciences, Beijing 100049, China

³Songshan Lake Materials Laboratory, Dongguan 523808, China

(Dated: February 28, 2025)

Various topological phases, including topological insulators, topological semimetals, and topological superconductors, along with the controllable topological phase transitions, have attracted considerable attention due to their promising applications in spintronics and quantum computing. In this work, we propose two distinct methods for manipulating topological phase transitions in magnetic materials. First, by varying the strength of electron correlation effects, we induce a series of topological state transitions within the EuM_2X_2 ($\text{M} = \text{Zn}, \text{Cd}; \text{X} = \text{P}, \text{As}, \text{Sb}$) family of Zintl materials, including magnetic topological crystalline insulators (TCIs) and magnetic Dirac semimetals. Our findings indicate that strong electron correlation effects tend to influence the emergence of topological phases. Second, by reducing the electronegativity of the pnictogen X (from P to As and Sb), we observe a similar transition from trivial insulator to magnetic Dirac semimetal or magnetic TCI. This suggests that weaker electronegativity favors the emergence of topological phases. Furthermore, we establish a Heisenberg model to describe the magnetic interactions of the EuM_2X_2 system, based on which we perform Monte Carlo simulations of specific heat and magnetic susceptibility, yielding Néel temperatures that perfectly match experimental data. This suggests that the local magnetic moment framework provides an accurate description of the magnetization behavior in this family of materials. This work provides the potential for the experimental manipulation of topological phase transitions and their possible applications, while also enhancing the understanding of the magnetic interactions within the EuM_2X_2 system and offering a theoretical foundation for future applications in magnetism.

I. INTRODUCTION

In recent decades, topological phases have drawn significant attention from condensed matter physicists due to their potential for dissipationless transport and their applications in quantum computation and spintronics [1–17]. As a result, identifying materials that host topological states and developing methods for controlling these states have become pivotal challenges in condensed matter physics. For materials with a band gap, the topological classification of the material and the corresponding edge states can generally be determined through the calculation of the topological invariants of the occupied states. A topological phase transition is typically accompanied by the closure of the energy gap. Therefore, the capability to control the process of gap opening and closing enables the manipulation of topological states. Previous studies have explored various approaches to induce and control topological phase transitions, including the application of strain[18], external electric fields[19], modification of magnetic configurations[20], adjustment of spin-orbit coupling strength[21, 22] and the tuning of interaction effects[23–25]. In this work, we simulate the effect of interaction strength on the topological phase transition by varying the Hubbard- U value, thereby enabling the control of the topological properties of the compound.

To analyze the process of topological phase transitions, the first step is to identify the topological phase of a given state. Due to the significant impact of symmetry on topological states, magnetic space groups (MSGs) are widely used in the study of topological phases in materials. By calculating the irreducible representations of the energy bands and

employing compatibility relations[26, 27], we can determine band degeneracies and identify band inversions. Additionally, symmetry indicator (SI) theory allows us to diagnose the topological properties of the system by calculating the eigenvalues of specific symmetry operations at high-symmetry points of the occupied states for a magnetic group[28–35].

Zintl-phase materials consist of metallic cations and anionic frameworks, where the metal cation donates electrons to the anionic framework, forming a strongly covalent anionic structure [36–38]. Due to their unique structure, Zintl phases exhibit both metallic and covalent characteristics, often leading to small band gaps. This feature allows spin-orbit coupling (SOC) to play a potentially significant role in determining the topological properties of these materials. Consequently, various topological states have been realized in Zintl phases, including topological insulators and Dirac semimetals, fueling substantial interest in their study [39–42]. For instance, in recent years, numerous experimental and theoretical studies have focused on the magnetic configurations and Néel temperature of EuCd_2As_2 , a compound generally believed to exhibit an A-type antiferromagnetic configuration with magnetic moments oriented along the in-plane a -axis (AFM-Aa) and a Néel temperature of approximately 9.5 K [12, 20, 43–49]. Above the Néel temperature, a competition between ferromagnetic and antiferromagnetic interactions is observed [49, 50]. When the magnetic moments are aligned in-plane, the compound behaves as a Z_2 TCI, whereas when the moments align along the c -axis, the compound exhibits Dirac semimetal behavior. This duality gives rise to the possibility of realizing multiple topological phases within a single compound [20].

Moreover, recent studies have demonstrated that the magnetic configuration of EuCd_2As_2 can be tuned via crystal growth techniques [51]. In multilayer EuCd_2As_2 , the quantum anomalous Hall (QAH) effect has been realized [52]. Additionally, EuM_2X_2 compounds have exhibited other intriguing properties, such as colossal magnetoresistance (CMR) [53–55], controllable anomalous Hall conductivity [56], and thermoelectric effects [57]. Clearly, Eu-based Zintl phases present complex and controllable magnetic interactions alongside diverse topological phases, providing opportunities for realizing various topological states in experiments. Furthermore, these materials exhibit numerous potentially exploitable physical properties, warranting further investigation.

In this study, we investigate the influence of electronic correlations and electronegativity on the topological states of Eu-based Zintl phases, as well as the mechanisms driving magnetic interactions within the EuM_2X_2 family of materials. Our findings reveal that strong electron correlation effects tend to influence the emergence of topological phases in these materials while the reduction in electronegativity promotes the appearance of topological phases. Moreover, we propose that the local magnetic moment framework offers an accurate description of the magnetization behavior in this family of materials.

II. METHOD

We performed first-principles calculations using the Vienna Ab-initio Simulation Package (VASP) [58, 59], with plane-wave basis sets and the Projector Augmented-Wave (PAW) method [60] to compute the electronic band structure. The exchange-correlation functional was described using the Perdew, Burke, and Ernzerhof (PBE) form under the Generalized Gradient Approximation (GGA) [61, 62]. To simulate the strong correlation effects of Eu- f electrons in the antiferromagnetic phase, we used the GGA+Hubbard- U (GGA+ U) approach [63]. To simulate the interaction-driven topological phase transitions, we varied the Hubbard- U parameter from 1 eV to 7 eV. The plane-wave cutoff energy was set to 500 eV, and the convergence criterion for total energy was set to 10^{-7} eV. For various magnetic configurations, we employed a Monkhorst-Pack k -point sampling scheme [64] with an $11 \times 11 \times 5$ k -point grid in the Brillouin zone. The effects of SOC were considered in all calculations. Irreducible representations and symmetry indicators were calculated using Irvsp[26].

We utilized the software WANNIER90 [65] to construct a tight-binding Hamiltonian model based on maximally localized Wannier functions (MLWFs). Taking EuZn_2As_2 with the AFM-Aa magnetic configuration as an example, the local Wannier orbital basis included the p orbitals of As, the s and p orbitals of Zn, and the s and d orbitals of Eu. The inner energy window spanned from 6 eV below to 6 eV above the Fermi level, while the outer energy window extended from 6 eV below to 15 eV above the Fermi level. We use the *postw90*

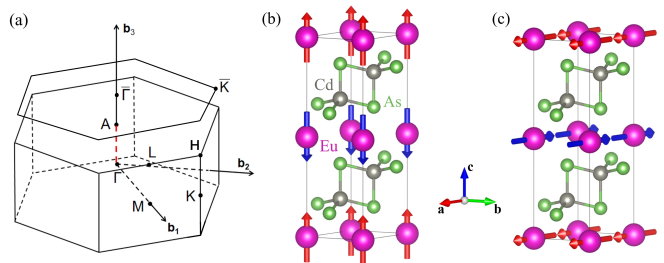


FIG. 1. (a) Schematic of the Brillouin Zone of EuCd_2As_2 (b) Magnetic structure of A-type AFM EuCd_2As_2 , with magnetic moment along c axis (AFM-Ac) (c) Magnetic structure of A-type AFM EuCd_2As_2 , with magnetic moment along a axis (AFM-Aa)

module in WANNIER90 [65] to implement the optical conductivity calculation where a $150 \times 150 \times 150$ k -mesh is employed. For simulations of temperature-dependent properties, including magnetic susceptibility and specific heat, we employed the Espins package [66], which relies on standard Monte Carlo methods. To calculate the surface states of the TCI, we applied the software WannierTools [67], which implements the iterative Green’s function method. A principal layer of two and an energy interval of 2000 slices were utilized in the calculation.

III. RESULTS AND DISCUSSION

A. Manipulation of topological phase transition

To explore the topological properties of the EuM_2X_2 family materials, we varied the Hubbard- U parameter from 1 eV to 7 eV to better capture the correlated interactions of the $4f$ electrons. It is well known that the $4f$ electrons in rare earth elements, especially lanthanides, are more localized than the outer $5p$ and $6s$ electrons. Thus, the correlation effects between electrons cannot be neglected, necessitating the inclusion of the Hubbard- U correction to accurately describe rare earth elements with $4f$ orbitals.

Here, we take EuCd_2As_2 as an example. Experimental data indicate that its magnetic configuration of ground state is AFM-Aa [46], as shown in Fig.1(c). Our calculations reveal that the energy of the magnetic configuration AFM-Ac is only 0.16 meV per magnetic unit cell, slightly higher than that of the magnetic configuration AFM-Aa. For comparison, we calculated the topological properties of the EuM_2X_2 series for both magnetic configurations with different U values.

The EuM_2X_2 family materials belong to space group $\text{P}\bar{3}m1$ (No. 164). Fig.1(a) shows the corresponding Brillouin zone and the high-symmetry points. When the magnetic moments of the Eu atoms align along the c -axis, forming the AFM-Ac magnetic configuration shown in Fig.1(b), the corresponding magnetic space group is $\text{P}c\bar{3}c1$ (No. 165.96)[27]. When the magnetic moments lie within the ab -plane, forming the AFM-Aa magnetic configuration shown in Fig.1(c), the correspond-

ing magnetic space group is C_c2/m (No. 12.63). Notice that, both the MSGs contain the inversion symmetry operation P combined with nonsymmorphic time-reversal symmetry $T*\tau$ operation, where τ represents a fractional translation along a lattice vector. As a result, the bands are doubly degenerate, protected by this symmetry.

Increasing U gradually simulates the process of increasing electron correlation interactions in the material. This is analogous to applying pressure to the material[68], resulting in the atoms moving closer, thereby enhancing electron correlation effects. Thus, tuning the Hubbard- U value to drive phase transitions has practical significance. Fig.2 illustrates the evolution of the EuCd_2As_2 band structure for both configurations as Hubbard- U increases. The most notable effect of increasing U on the band structure is the gradual downward shift of the occupied $4f$ electron states. Orbital projection analysis reveals that the primary orbital components near the Fermi level are the p orbitals of As and the s orbitals of Cd (see Supplemental Material Fig.S1).

Topological quantum chemistry and symmetry indicators have emerged in recent years as powerful tools for analyzing the topological classification of compounds. These methods are highly useful in facilitating high-throughput searches for topological materials[28–35]. In addition to analyzing the relative positions of bands and corresponding band inversions, we also calculated the SI, Z'_{2p} , for different U values based on the parity of all occupied states below the Fermi level, as described in [34]:

$$Z'_{2p} = \sum_{k \in \text{TRIM}} \frac{1}{4} (N_k^- - N_k^+) \pmod{2}. \quad (1)$$

We notice that the presence of a significant gap within the occupied states, so we only need to count the parity information of the states between the gap and the Fermi level. Note that, through the analysis of the representation of MSG for both magnetic configuration, among the eight time-reversal invariant momenta (TRIM) in the Brillouin zone, all band pairs at four points in the $k_z = \pi/c$ are energy-degenerate with opposite parity eigenvalues, and thus do not contribute to the Z_2 index. Therefore, we only need to consider the four points in the $k_z = 0$ plane in the following analysis. Notably, in the following discussion, each pair of doubly degenerate bands is assigned a single parity eigenvalue.

For the AFM-Aa magnetic configuration of EuCd_2As_2 , we present the band structure near the Γ point in the vicinity of the Fermi level in Fig.3, along with the parity eigenvalues of each band at the Γ point and the eigenvalues of C_2 operation at the A point (where $+i$ is denoted as $+$, and $-i$ as $-$). Since only one representation, $B3 + B4$, exists along the Γ -A path, there is no crossing between the conduction and valence bands, ensuring a gap. Thus, to analyze the topological transition, we focus only on the number of bands below the Fermi level with positive parity at the Γ point. We observe that there is a change in the number of bands with positive parity below the Fermi level at the Γ point as U increases from 1 eV to 2

eV. This corresponds to a topological phase transition from a trivial insulator to a Z_2 TCI. As U increases to 3, 4, and 5 eV, the number of occupied states with positive parity at the Γ point remains unchanged. However, when U increases from 5 eV to 6 eV, a second change in the number of occupied states with positive parity at the Γ point occurs, indicating a phase transition from a TCI back to a trivial insulator. The specific parity eigenvalues at each point are shown in TableI.

TABLE I. The number of occupied bands with positive parity eigenvalues among the four high symmetry k points at $k_z = 0$ within the Brillouin zone for the AFM-Ac and AFM-Aa magnetic configurations of EuCd_2As_2 , below the Fermi energy, along with their corresponding topological classifications at varying values of U .

U (eV)	AFM-Ac			AFM-Aa		
	Γ	3M	CLASS	Γ	Y	2V CLASS
1	8	6	Trivial	8	6	6 Trivial
2	7	6	TCI	7	6	6 TCI
3	7	6	TCI	7	6	6 TCI
4	7	6	Dirac	7	6	6 TCI
5	6	6	Trivial	7	6	6 TCI
6	6	6	Trivial	6	6	6 Trivial
7	6	6	Trivial	6	6	6 Trivial

In Fig.4, we present the band structure near the Γ point for EuCd_2As_2 with magnetic configuration AFM-Ac, along with the bands with positive parity eigenvalues near the Fermi level at the Γ point, and the corresponding representations of the bands along the high-symmetry Γ -A path. Similarly, as U increases from 1 eV to 7 eV, the number of bands below the Fermi level with positive parity at the Γ point decreases from 8 to 7, and then to 6. This indicates that two band inversions occur as U rises. Consistently, the calculations of SI show that at $U = 1$ eV, the compound is a trivial insulator; at $U = 2$ and 3 eV, it is a Z_2 TCI; at $U = 4$ eV, becomes a Dirac semimetal; and at $U = 5, 6,$ and 7 eV, the compound returns to a trivial insulator. The specific parity transformations are listed in TableI. In the following, we present a detailed description of the band inversion process as the Hubbard- U value increases.

As U increases from 1 eV to 2 eV: The second band below the Fermi level at $U = 1$ eV (labeled as DT6 along the Γ -A path, with a positive parity eigenvalue at the Γ point) exchanges order with the two bands above it, resulting in the first band above the Fermi level at $U = 2$ eV having a positive parity eigenvalue at the Γ point. The first band below the Fermi level at $U = 1$ eV moves up and intersects with the first band above it. Due to the different representations of the two bands, no gap opens at the intersection, as shown in Fig.4(b). The fourth band below the Fermi level at $U = 1$ eV (labeled as DT6 along the Γ -A path, with a positive parity eigenvalue at the Γ point) undergoes a band inversion at the Γ point with the band above it. Since both bands along the Γ -A path are labeled as DT6, a gap opens at the band crossing, as shown by the third band below the Fermi level in Fig.4(b).

As U increases from 2 eV to 3 eV: The first and second bands above the Fermi level at $U = 2$ eV undergo a band in-

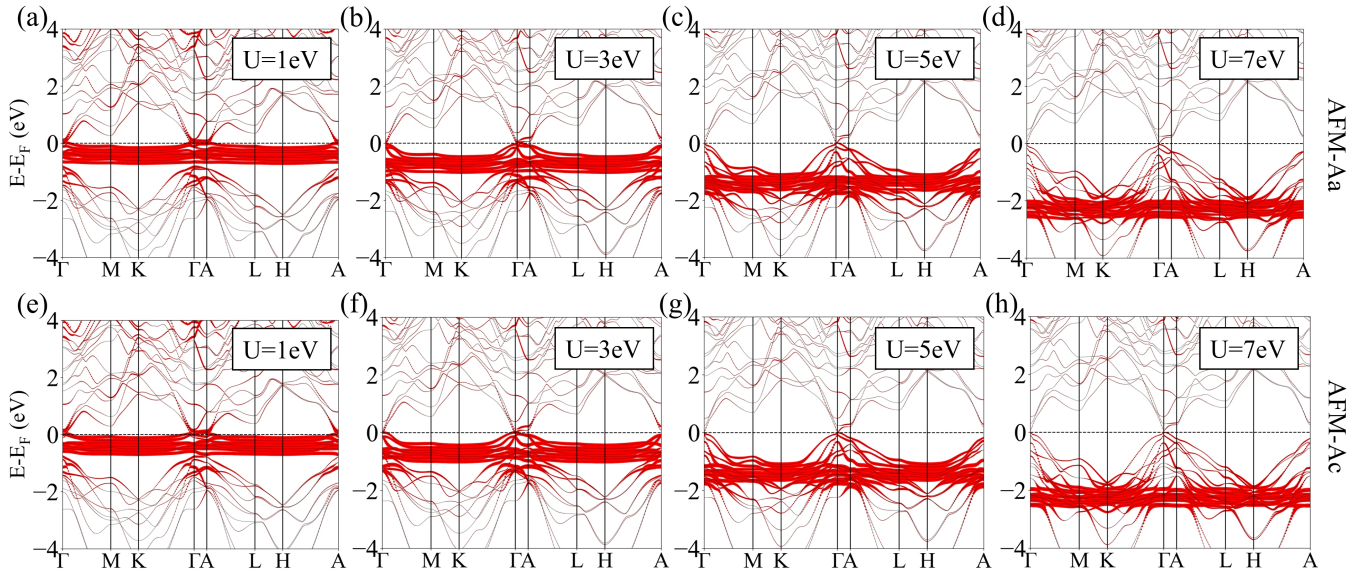


FIG. 2. Band Structure and Eu- $4f$ Orbital Projection of EuCd_2As_2 . Effective Hubbard- U interactions of 1, 3, 5, and 7 eV were applied in the calculations for panels (a)-(d), corresponding to the AFM-Aa magnetic configuration, and for panels (e)-(h), corresponding to the AFM-Ac configuration.

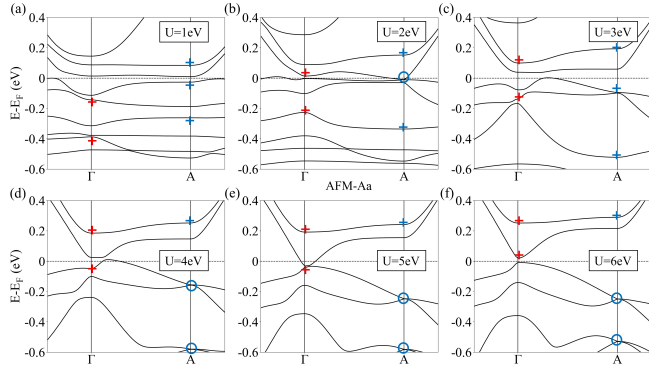


FIG. 3. Band structure of EuCd_2As_2 with the AFM-Aa magnetic configuration along the Γ -A path. Panels (a) to (f) depict the evolution of band structures for Hubbard- U values from 1 to 6 eV. The band structure for $U = 7$ eV is omitted as it closely resembles that of $U = 6$ eV. Bands at the Γ point with positive parity eigenvalues are marked with red plus signs, while those at the A point with eigenvalue i of the C_2 operation are denoted by blue plus signs. Degenerate bands with both i and $-i$ eigenvalues of the C_2 operation are represented by blue circles.

version at the Γ point. Since both bands are labeled as DT6, no crossing appears along the Γ -A path. The third and the second band below the Fermi level undergo a band inversion at the Γ point. Similarly, no crossing appears along the Γ -A path since both bands share the same DT6 representation.

As U increases from 3 eV to 4 eV: The first band above the Fermi level at $U = 3$ eV (with negative parity eigenvalue at the Γ point) undergoes a band inversion with the first band below the Fermi level (also with negative parity eigenvalue at the Γ point), and the first and second band below the Fermi

level approximately intersect at the Γ point. Since the bands above and below the Fermi level have different representations at $U = 4$ eV, a band crossing occurs between the conduction and valence bands during the band inversion. As previously mentioned, the presence of the combined P and $T * \tau$ symmetry ensures that each band is doubly degenerate. Therefore, the crossing point here is a fourfold degenerate point, also known as a Dirac point illustrated by an orange circle in Fig.4(d). Meanwhile, the first and second bands below the Fermi level exchange order at A, lifting the degeneracy along the Γ -A path.

As U increases from 4 eV to 7 eV: The two energy bands which give rise to the Dirac point at $U = 4$ eV gradually separate until the Dirac point disappears, resulting in a positive parity eigenvalue for the first energy band above the Fermi surface at the Γ point. The band structure of $U = 7$ eV is almost identical to that of $U = 6$ eV, so it is omitted from the figure.

To further investigate the surface states of TCI, we consider the AFM-Aa magnetic configuration of EuCd_2As_2 as an illustrative example. Among the EuM_2X_2 series, the AFM-Aa configuration of EuCd_2As_2 exhibits the most significant band gaps, making it an ideal candidate for visualizing surface states. As shown in [34], the non-trivial SI, Z'_{2p} signifies the presence of non-trivial topological invariants originating from mirror symmetry and anti-unitary translation symmetry operations. These invariants give rise to surface states in the surface Brillouin zone perpendicular to the mirror plane. A Dirac cone forms along the mirror-invariant high-symmetry line, which corresponds to the intersection of the surface Brillouin zone with the mirror plane in the 3D Brillouin zone. Due to the opposite mirror Chern numbers of two groups of bands

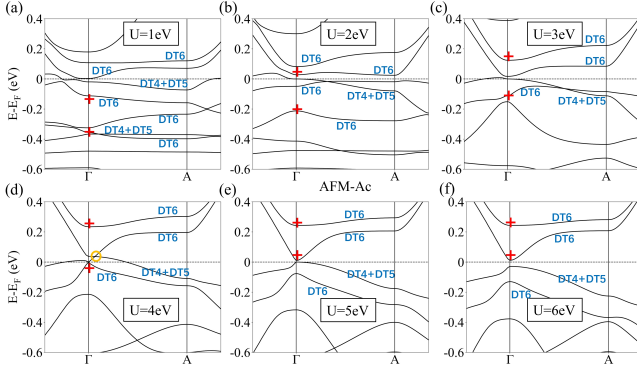


FIG. 4. Band Structure along the Γ -A path for EuCd_2As_2 with the AFM-Ac magnetic configuration. (a)-(f) correspond to Hubbard- U values ranging from 1 to 6 eV, with the band structure for $U = 7$ eV being nearly identical to that for $U = 6$ eV and thus omitted here. The bands at the Γ point with positive parity eigenvalues are indicated by red plus signs. Additionally, (b)-(d) show the representations along the Γ -A path for the bands that cross near the Fermi level.

with different mirror symmetry eigenvalues, the surface states manifest as a Dirac cone in the surface Brillouin zone rather than as chiral edge states.

In this primitive unit cell setting, the mirror plane is M_{100} . To investigate the surface state, we calculated the band structure along the $\bar{K} - \bar{\Gamma} - \bar{K}$ path in the surface Brillouin zone, explicitly revealing the existence of the surface states. As shown in Table I and Fig.3, the compound is a TCI for $U = 3, 4,$ and 5 eV, and transitions to a trivial insulator when $U = 6$ eV. Notably, at $U = 3$ eV, the band gap is as large as 50 meV, which facilitates the observation of surface states, as shown in Fig.5(a). For $U = 4$ eV, the band gap is smaller, yet the surface states remain discernible, as depicted in Fig.5(b). At $U = 6$ eV, the compound becomes a trivial insulator. Although a clear gap is observed in Fig.5(c), no surface states are present, aligning perfectly with the SI analysis described above.

It is worth noting that we observe that the first and second bands below the Fermi level at the A point appear to be 'degenerate' for U values between 4 and 6 eV, as illustrated by a blue circle in Fig.3(d)-(f). This 'degeneracy' can also be found between the conduction and valence bands at the A point for $U = 2$ in Fig.3(b). Due to the combined symmetry of $T * \tau$ and P in this material ensuring that every band is doubly degenerate, the point where the first and second bands below the Fermi level meet forms a fourfold 'degeneracy'. The MSG of EuCd_2As_2 in this magnetic configuration is C_c2/m (No. 12.63), which has two representations at A, namely $A3+A5$ and $A4+A6$, both of which are two-dimensional representations. This is inconsistent with the MSG representations, which only allow for twofold degeneracies. What causes this discrepancy?

Taking the 'degeneracy' between the conduction and valence bands at the A point in Fig.3(d) as an example, we find that these seemingly degenerate bands actually exhibit an energy splitting of 0.12 meV at A, indicating that they are

not truly degenerate. This confirms the consistency of the MSG representation analysis. However, we find that such approximate fourfold degeneracies, or very small energy splittings at high-symmetry points, are not coincidental in the band structures shown in Fig.3. We believe that the theory of spin space group (SSG) [69, 70] can explain the occurrence of these approximate fourfold degeneracies. The MSG describes magnetic systems with SOC, whereas SSG is established to describe magnetic systems without SOC. When the effect of SOC is very weak, the energy contribution of SOC can be treated as a perturbation. Consequently, we can use SSG representations to analyze systems with weak SOC. Through calculations, we find that the SSG of this material is 164.2.1.1.L [70], which has six different representations at A, two of which are four-dimensional, and four of which are two-dimensional. This suggests that if we ignore SOC, the aforementioned approximate fourfold degeneracy would be a true fourfold degeneracy.

Furthermore, we have calculated the topological classifications of other materials in the EuM_2X_2 family materials with varying U , as shown in Table II. Overall, as the Hubbard- U increases, the increasing correlation interaction among Eu-4*f* electrons manifests in the band structure as an increasing energy difference between the unoccupied 4*f* orbitals and the occupied 4*f* orbitals, as shown in Fig.2. The energy of the occupied Eu-4*f* electrons decreases with increasing U , which is one driving factor for the band inversion. In summary, by reducing the electronegativity of the pnictogen element X, we enabled the transition from a trivial insulator to a magnetic Dirac semimetal or a magnetic TCI. Moreover, by analyzing the representations along high-symmetry paths for different magnetic configurations, we find that the symmetry operations in MSG constrain the appearance of possible topological phases, demonstrating that magnetic configurations play a crucial role in their topological classification. We will elaborate on the magnetic interactions of the EuM_2X_2 family materials in the following sections.

When comparing the band structures obtained from calculations and experiments for a given material, one specific Hubbard- U value is typically the most suitable. For example, in previous research on Eu-based Zintl-phase materials, Hubbard- U values ranging from 3.1 eV to 6.3 eV have been adopted [44, 52, 71–73]. Using EuZn_2As_2 with magnetic configuration AFM-Aa as an example, by comparing the optical conductivity obtained from calculations with experimental transmission results, we find when U is set to 5 eV, the peaks in optical conductivity match the bottom of transmission spectrum around the wave number of 2700 cm^{-1} [74] very well (see Supplemental Material Fig.S2). Therefore, we use a Hubbard- U of 5 eV in the comparative study of the EuM_2X_2 series of materials, to control variables effectively.

In Fig.6, we present the band structures of the EuM_2X_2 series materials with magnetic configuration AFM-Aa at $U = 5$ eV. From top to bottom and left to right, both M and X atoms are arranged from lighter to heavier. Firstly, comparing the

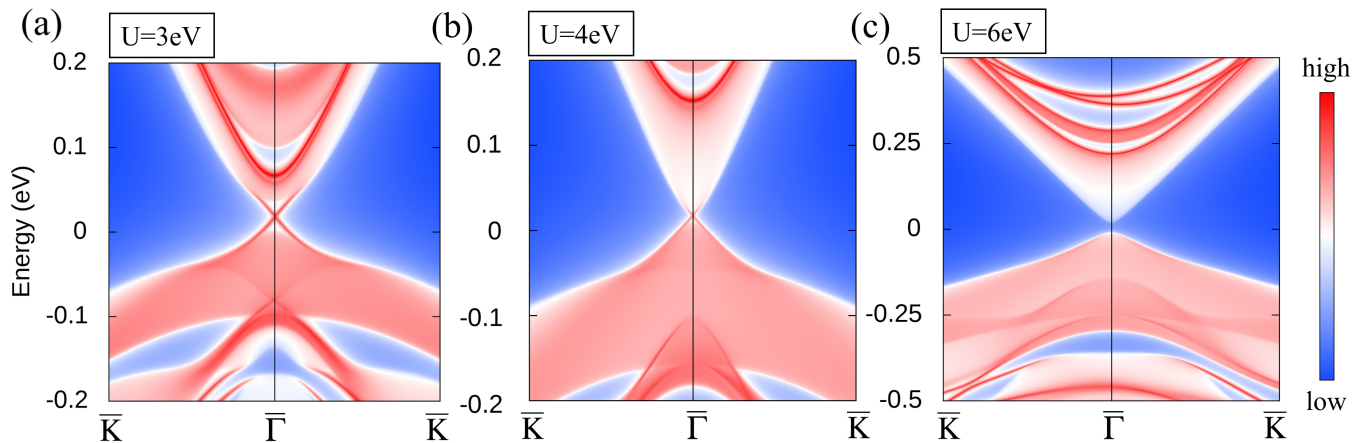


FIG. 5. Surface states of EuCd_2As_2 with AFM-Aa configuration for Hubbard U values of 3, 4 and 6 eV

TABLE II. Topological classification of AFM-Ac and AFM-Aa magnetic configuration of EuCd_2As_2 series compounds at varying values of U .

Material	Magnetic Configuration	$U=1$ eV	$U=2$ eV	$U=3$ eV	$U=4$ eV	$U=5$ eV	$U=6$ eV	$U=7$ eV
EuZn_2P_2	AFM-Ac	Trivial						
EuZn_2P_2	AFM-Aa	Trivial						
EuZn_2As_2	AFM-Ac	TCI	TCI	Dirac	Dirac	Trivial	Trivial	Trivial
EuZn_2As_2	AFM-Aa	TCI	TCI	TCI	TCI	Trivial	Trivial	Trivial
EuZn_2Sb_2	AFM-Ac	TCI	TCI	Dirac	Dirac	Dirac	Dirac	Dirac
EuZn_2Sb_2	AFM-Aa	TCI						
EuCd_2P_2	AFM-Ac	Trivial						
EuCd_2P_2	AFM-Aa	Trivial						
EuCd_2As_2	AFM-Ac	Trivial	TCI	TCI	Dirac	Trivial	Trivial	Trivial
EuCd_2As_2	AFM-Aa	Trivial	TCI	TCI	TCI	TCI	Trivial	Trivial
EuCd_2Sb_2	AFM-Ac	TCI	TCI	TCI	TCI	Dirac	Dirac	Dirac
EuCd_2Sb_2	AFM-Aa	TCI						

two rows, we observe that the substitution of the atom M has a minimal impact on the band structure. In contrast, a comparison of the three columns from left to right reveals a notable change in the band structure. Specifically, as the atom X becomes heavier, the band gap between the conduction and valence bands decreases gradually. When X is P, a distinct band gap exists between the conduction band and the valence band. As X transitions to As, the band gap nearly vanishes, and when X is Sb, the band structure exhibits a 'negative band gap'. We attribute this significant decrease in the band gap from element substitution to differences in their electronegativity. For ionic crystals (e.g. NaCl), the band gap is often large due to the pronounced effect of the transfer of electrons between atoms. In contrast, in covalent compounds, the electron transfer is less pronounced, leading to a smaller band gap at the Fermi level. As the atom X changes from P to As and Sb, its electronegativity reduces. Consequently, the difference in electronegativity between the atom X and the atom Eu or M also reduces. This increase in covalent character of the chemical bonds results in a transition from a positive band gap to a zero band gap and eventually to a negative band gap.

B. Mechanisms of magnetic interactions in EuM_2X_2

In previous studies, the investigation of magnetic configurations and the Néel temperature of the EuM_2X_2 system has been a prominent topic [46, 49, 75–82]. Taking EuCd_2As_2 as an example, previous studies have shown some controversy regarding its ground-state magnetic configuration, however, it is now generally accepted that its ground state adopts the AFM-Aa magnetic configuration. We summarize the Néel temperatures of various materials in the EuM_2X_2 series, as shown in Table III [43, 45, 76, 83–89]. Observations show that, when the atom M is fixed, the Néel temperature decreases as the atom X transitions from P to As and Sb, indicating a reduction in the stability of the magnetic interactions. To explore the fundamental reason for this trend, we establish a basic Heisenberg model that includes both in-plane and out-of-plane magnetic interactions:

$$H_{\text{eff}} = - \sum_{\langle i,j \rangle} J_{\parallel} \hat{\mathbf{S}}_i \cdot \hat{\mathbf{S}}_j - \sum_{\langle\langle i',j' \rangle\rangle} J_{\perp} \hat{\mathbf{S}}_{i'} \cdot \hat{\mathbf{S}}_{j'}. \quad (2)$$

where J_{\parallel} represents the exchange parameter within the ab

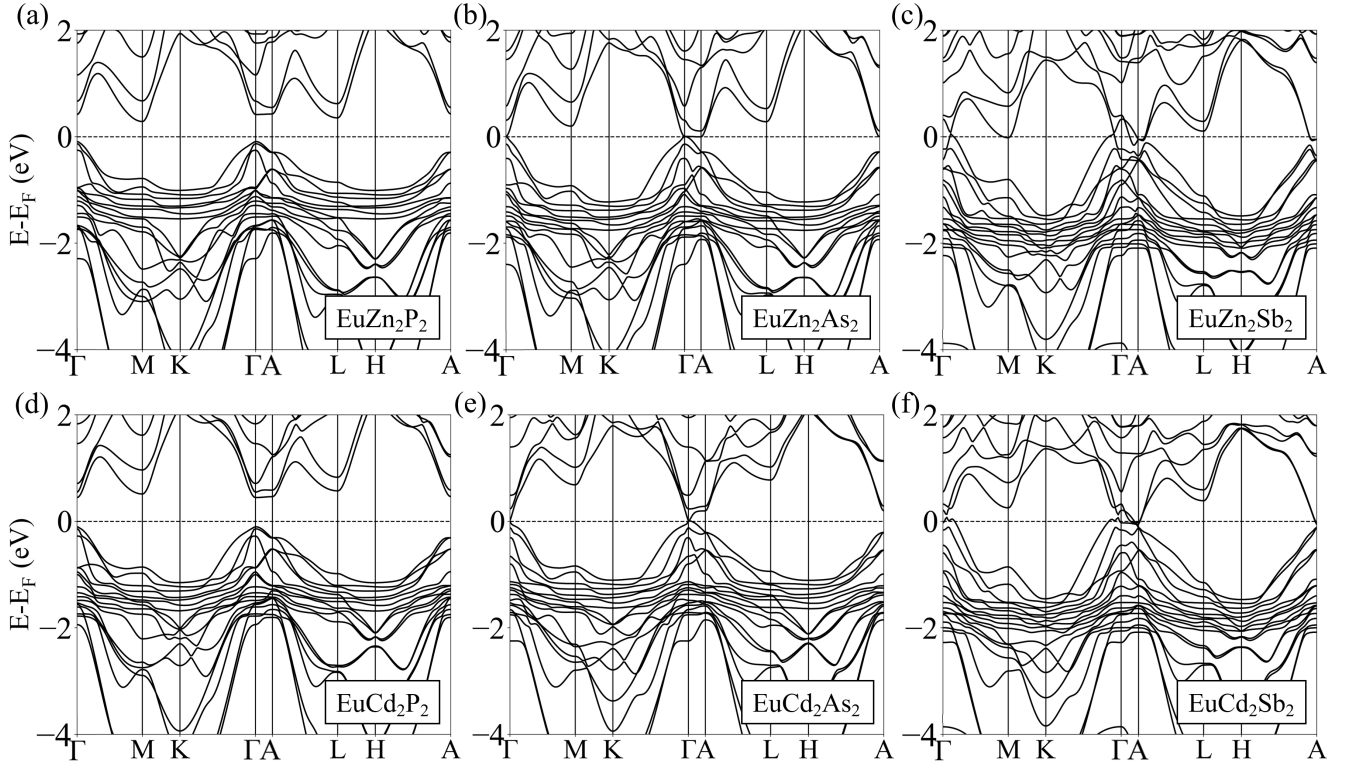


FIG. 6. Comparison of band structures for EuM_2X_2 series materials with AFM-Aa configuration when effective Hubbard interaction of $U=5$ eV is applied.

TABLE III. Comparison of ground state energies of various magnetic configurations, convergence tolerances, exchange parameters, and Néel temperatures for EuM_2X_2 series compounds. (Note that, 'Exp' represents the experimental data, 'Cp' represents the results derived from heat capacity simulation and ' χ ' represents the results derived from susceptibility simulation.)

	EuZn ₂ P ₂	EuZn ₂ As ₂	EuZn ₂ Sb ₂	EuCd ₂ P ₂	EuCd ₂ As ₂	EuCd ₂ Sb ₂
AFM (eV)	-211.297414	-197.947976	-181.676900	-198.008644	-190.895111	-177.460445
AFM' (eV)	-211.279861	-197.933956	-181.668696	-197.998412	-190.890047	-177.457724
FM (eV)	-211.285872	-197.930864	-181.657084	-197.997200	-190.890725	-177.452341
FM' (eV)	-211.274085	-197.925336	-181.658776	-197.992688	-190.887789	-177.453747
Tolerance (eV)	5×10^{-6}	7×10^{-5}	1×10^{-5}	3×10^{-6}	3×10^{-5}	7×10^{-5}
J_{\parallel} (meV)	1.22	0.812	0.271	0.614	0.334	0.0579
J_{\perp} (meV)	-0.721	-1.07	-1.24	-0.715	-0.274	-0.506
T_N [Exp] (K)	23	19	12	11	9.5	7.8
T_N [Cp] (K)	23.65	20.00	10.60	14.57	7.05	3.09
T_N [χ] (K)	25.43	21.46	11.86	15.82	7.58	3.71

plane, and J_{\perp} is the exchange parameter along the c direction, as shown in Fig.7(a). i, j and i', j' represent the nearest neighbor and next nearest neighbor, respectively. To determine J_{\parallel} and J_{\perp} , we calculated the ground state energies for four magnetic configurations[80, 90, 91] : (a) the antiferromagnetic configuration (AFM), (b) the AFM configuration with the spin of a randomly selected atom reversed (AFM'), (c) the ferromagnetic configuration (FM), and (d) the FM configuration with the spin of a randomly selected atom reversed (FM') as shown in Fig.7.

Notably, we solve for three variables namely: J_{\parallel} , J_{\perp} and the reference energy E_0 using four equations, making it an

overdetermined system. Thus, we use the variables derived from first three configurations to verify the ground-state energy of the fourth configuration. The ground-state energy of the fourth configuration calculated in this way, shows negligible deviation from the value obtained through first-principles calculations, indicating that the overdetermined system of equations is self-consistent. To clarify, we have also listed the self-consistent tolerance for each compound in TableIII. As shown in TableIII, we notice that the exchange parameter within the ab plane J_{\parallel} , is considerably small when $X = \text{Sb}$, we attribute this to the distance between Eu atoms in the ab plane is 4.494 and 4.698 in EuZn_2Sb_2 and

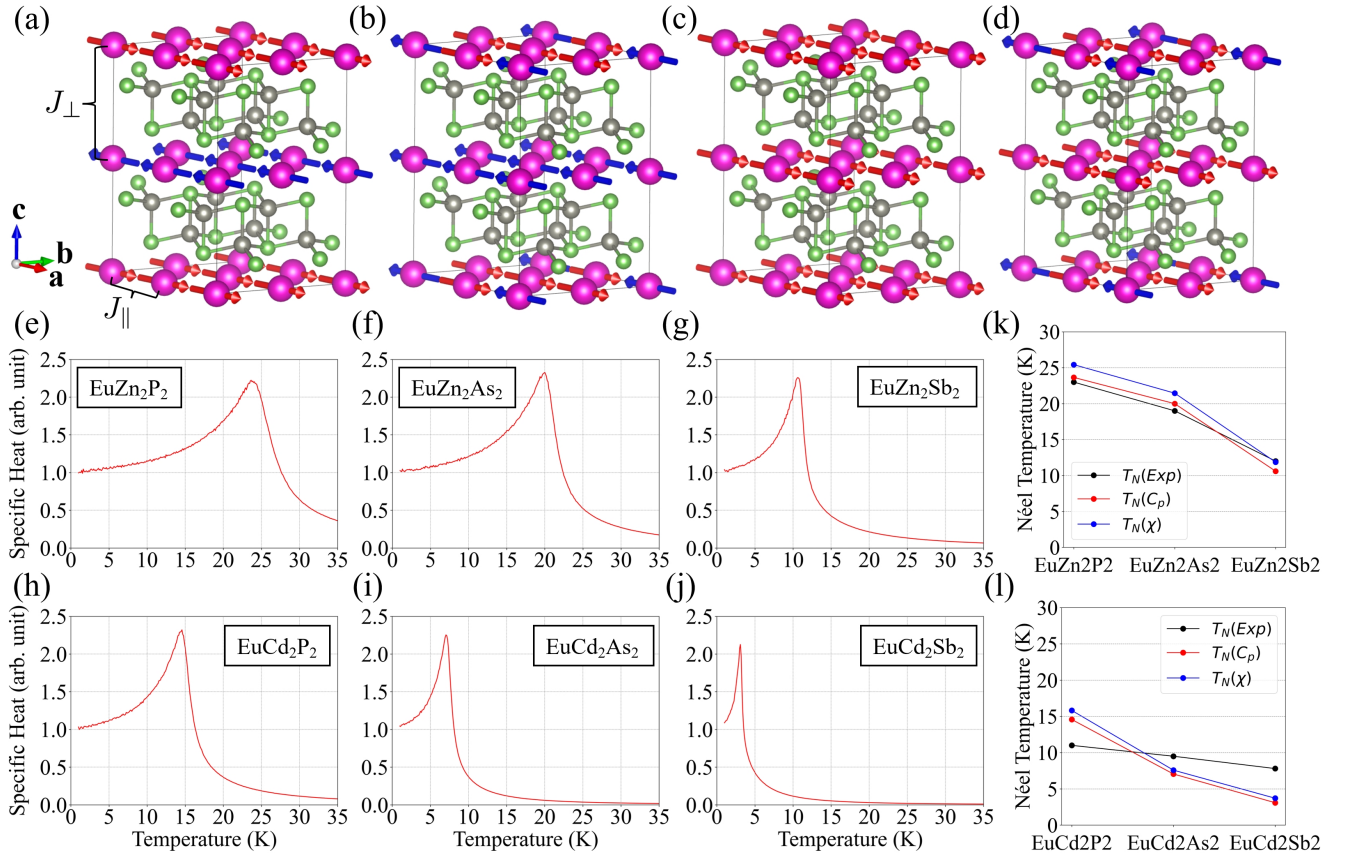


FIG. 7. Panels (a)-(d) display the magnetic unit cells of EuM_2X_2 with distinct magnetic configurations: AFM, AFM', FM, and FM'. The temperature dependence of the heat capacity for the EuM_2X_2 series is presented in panels (e)-(j). Panels (k)-(l) offer a comparative overview of the Néel temperature, juxtaposing theoretical predictions with experimental results for both the EuZn_2X_2 and EuCd_2X_2 series. In these figures, black points represents the experimental data, red points corresponds to theoretical calculations based on heat capacity, and blue points signifies those derived from susceptibility data.

EuCd_2Sb_2 [85, 86, 88, 89], respectively, larger than that of the other materials in EuM_2X_2 series [43, 45, 76, 83, 84, 87].

Using J_{\parallel} and J_{\perp} obtained above, we performed standard Monte Carlo simulations [66] to calculate the temperature dependence of the heat capacity and magnetization of each material in EuM_2X_2 . A peak is clearly observed in these curves, indicating that the material undergoes a phase transition at this temperature which corresponds to the Néel temperature. Table III provides a summary of the Néel temperatures for each material, while Fig. 7(k)(l) illustrate these values graphically. In these figure, black points denotes the experimental data, whereas red and blue points indicate Monte Carlo simulation Néel temperature results derived from heat capacity and susceptibility data, respectively. Notably, the Néel temperatures calculated using a two-parameter Heisenberg model agree very well with the experimental results. For a system with controversial magnetic configurations [46, 49], this is an interesting development. This indicates that our Heisenberg model captures the underlying physical nature of the magnetic interactions in the EuM_2X_2 series, providing a crucial foundation for future research. Meanwhile, we also derived the Néel temperatures of EuCd_2Sb_2 from the calculation with different

Hubbard- U value, which are 13.00 K when $U = 3$ eV, 7.05 K when $U = 5$ eV and 3.30 K when $U = 7$ eV. By comparison, we found the Néel temperature of $U = 5$ eV is in close agreement with the experimental value of 9.5 K, indicating the choice of $U = 5$ eV in the above calculation is reasonable. This is further supported by the comparison of optical conductivity presented in the Supplemental Material as illustrated above.

IV. CONCLUSION

In summary, we conducted a comprehensive first-principles calculation and magnetic Monte Carlo simulation study on the EuM_2X_2 family of materials, resulting in two distinct approaches for topological manipulation, while also elucidating the mechanisms of magnetic interactions within the EuM_2X_2 compounds. Firstly, we simulated the strength of electron correlation effects in the materials, which can be experimentally controlled through approaches such as applying pressure, by altering the Hubbard- U parameter in the calculation. We found that the strength of electron correlation significantly influences the topological properties of the materials, enabling

topological manipulation. Using EuM_2X_2 with magnetic configuration AFM-Ac as an example, we observed that as the Hubbard- U value increased from 1 eV to 6 eV, the compound underwent multiple topological phase transitions, evolving from trivial insulator to TCI, then to Dirac semimetal, and finally returning to trivial insulator. This provides a promising platform for realizing multiple topological states within a single material. Secondly, in EuM_2X_2 , as the element X is replaced sequentially from P to As and then to Sb, there is an increase in covalent character, leading to a transition from a positive band gap to a negative one. This alters the sum of parity eigenvalues of valence states and corresponding topological classification. As the weight of element X increases, the EuM_2X_2 compound transitions from a trivial insulator to a TCI. This represents a second approach to achieving topological manipulation through elemental substitution. Moreover, using the magnetic exchange coefficients derived from the 'four-state method', we performed Monte Carlo simulations, yielding Néel temperatures that closely match experimental data. This indicates that the model we proposed regarding nearest-neighbor magnetic interactions effectively describe the magnetic interactions within EuM_2X_2 family of Zintl materials, paving the way for manipulating magnetic structures and potential future applications in magnetism.

ACKNOWLEDGMENT

We would like to thank Dr. Z.Y. Liao and Z.Q. Guan of the Institute of Physics, Chinese Academy of Sciences, Dr. Y. Jiang of Donostia International Physics Center, Paseo Manuel de Lardizábal and Prof. A. Ptok, Dr. S. Dan of the Institute of Nuclear Physics, Polish Academy of Science, for helpful discussions. The authors acknowledge the support from the National Key Research and Development Program of China (Grant No. 2022YFA1403800), the National Natural Science Foundation of China (Grants No. 12188101, 11925408), the Chinese Academy of Sciences (Grant No. XDB33000000), and the New Cornerstone Science Foundation through the XPLORER PRIZE.

* hmweng@iphy.ac.cn

- [1] Haijun Zhang, Chao-Xing Liu, Xiao-Liang Qi, Xi Dai, Zhong Fang, and Shou-Cheng Zhang, "Topological insulators in Bi_2Se_3 , Bi_2Te_3 and Sb_2Te_3 with a single Dirac cone on the surface," *Nature Physics* **5**, 438–442 (2009).
- [2] Liang Fu and C. L. Kane, "Topological insulators with inversion symmetry," *Phys. Rev. B* **76**, 045302 (2007).
- [3] C. L. Kane and E. J. Mele, " \mathbb{Z}_2 topological order and the quantum spin hall effect," *Phys. Rev. Lett.* **95**, 146802 (2005).
- [4] K. v. Klitzing, G. Dorda, and M. Pepper, "New method for high-accuracy determination of the fine-structure constant based on quantized hall resistance," *Phys. Rev. Lett.* **45**, 494–497 (1980).
- [5] Jiaheng Li, Yang Li, Shiqiao Du, Zun Wang, Bing-Lin Gu, Shou-Cheng Zhang, Ke He, Wenhui Duan, and Yong Xu, "Intrinsic magnetic topological insulators in van der waals layered mnbi2te4-family materials," *Science Advances* **5**, eaaw5685 (2019).
- [6] F. D. M. Haldane, "Model for a quantum hall effect without landau levels: Condensed-matter realization of the "parity anomaly"," *Phys. Rev. Lett.* **61**, 2015–2018 (1988).
- [7] Hongming Weng, Chen Fang, Zhong Fang, B. Andrei Bernevig, and Xi Dai, "Weyl semimetal phase in noncentrosymmetric transition-metal monophosphides," *Phys. Rev. X* **5**, 011029 (2015).
- [8] S. M. Young, S. Zaheer, J. C. Y. Teo, C. L. Kane, E. J. Mele, and A. M. Rappe, "Dirac semimetal in three dimensions," *Phys. Rev. Lett.* **108**, 140405 (2012).
- [9] Zhijun Wang, Yan Sun, Xing-Qiu Chen, Cesare Franchini, Gang Xu, Hongming Weng, Xi Dai, and Zhong Fang, "Dirac semimetal and topological phase transitions in A_3Bi ($a = \text{Na}, \text{K}, \text{rb}$)," *Phys. Rev. B* **85**, 195320 (2012).
- [10] Zhijun Wang, Hongming Weng, Quansheng Wu, Xi Dai, and Zhong Fang, "Three-dimensional dirac semimetal and quantum transport in cd_3as_2 ," *Phys. Rev. B* **88**, 125427 (2013).
- [11] Peizhe Tang, Quan Zhou, Gang Xu, and Shou-Cheng Zhang, "Dirac fermions in an antiferromagnetic semimetal," *Nature Physics* **12**, 1100–1104 (2016).
- [12] Guiyuan Hua, Simin Nie, Zhida Song, Rui Yu, Gang Xu, and Kailun Yao, "Dirac semimetal in type-iv magnetic space groups," *Phys. Rev. B* **98**, 201116 (2018).
- [13] P. Dziawa, B. J. Kowalski, K. Dybko, R. Buczko, A. Szczepakow, M. Szot, E. Łusakowska, T. Balasubramanian, B. M. Wojek, M. H. Berntsen, O. Tjernberg, and T. Story, "Topological crystalline insulator states in $\text{pb}_1\text{-xsnxse}$," *Nature Materials* **11**, 1023–1027 (2012).
- [14] Yoichi Ando and Liang Fu, "Topological crystalline insulators and topological superconductors: From concepts to materials," *Annual Review of Condensed Matter Physics* **6**, 361–381 (2015).
- [15] Liang Fu, "Topological crystalline insulators," *Phys. Rev. Lett.* **106**, 106802 (2011).
- [16] Y. Tanaka, Zhi Ren, T. Sato, K. Nakayama, S. Souma, T. Takahashi, Kouji Segawa, and Yoichi Ando, "Experimental realization of a topological crystalline insulator in snte ," *Nature Physics* **8**, 800–803 (2012).
- [17] Timothy H. Hsieh, Hsin Lin, Junwei Liu, Wenhui Duan, Arun Bansil, and Liang Fu, "Topological crystalline insulators in the SnTe material class," *Nature Communications* **3**, 982 (2012).
- [18] Lars Winterfeld, Luis A. Agapito, Jin Li, Nicholas Kioussis, Peter Blaha, and Yong P. Chen, "Strain-induced topological insulator phase transition in hgse ," *Phys. Rev. B* **87**, 075143 (2013).
- [19] Jing-Yang You, Xue-Juan Dong, Bo Gu, and Gang Su, "Electric field induced topological phase transition and large enhancements of spin-orbit coupling and curie temperature in two-dimensional ferromagnetic semiconductors," *Phys. Rev. B* **103**, 104403 (2021).
- [20] Junzhang Ma, Han Wang, Simin Nie, Changjiang Yi, Yuanfeng Xu, Hang Li, Jasmin Jandke, Wulf Wulfhekel, Yaobo Huang, Damien West, Pierre Richard, Alla Chikina, Vladimir N. Strocov, Joël Mesot, Hongming Weng, Shengbai Zhang, Youguo Shi, Tian Qian, Ming Shi, and Hong Ding, "Emergence of nontrivial low-energy dirac fermions in antiferromagnetic eucd_2as_2 ," *Advanced Materials* **32**, 1907565 (2020).
- [21] Liqin Zhou, Zhiyun Tan, Dayu Yan, Zhong Fang, Youguo Shi, and Hongming Weng, "Topological phase transition in the lay-

- ered magnetic compound mnsb_2te_4 : Spin-orbit coupling and interlayer coupling dependence,” *Phys. Rev. B* **102**, 085114 (2020).
- [22] Liqin Zhou, Yuting Qian, Changming Yue, Yi Jiang, Zhong Fang, Wei Zhang, Chen Fang, and Hongming Weng, “Topological states and topological phase transition in Cu_2SnS_3 and Cu_2SnSe_3 ,” *Phys. Rev. Res.* **4**, 033067 (2022).
- [23] Xiangang Wan, Ari M. Turner, Ashvin Vishwanath, and Sergey Y. Savrasov, “Topological semimetal and fermi-arc surface states in the electronic structure of pyrochlore iridates,” *Phys. Rev. B* **83**, 205101 (2011).
- [24] Mohsen Hafez-Torbati, Jun-Hui Zheng, Bernhard Iršigler, and Walter Hofstetter, “Interaction-driven topological phase transitions in fermionic $\text{su}(3)$ systems,” *Phys. Rev. B* **101**, 245159 (2020).
- [25] Yuefang Hu, Changming Yue, Danwen Yuan, Jiacheng Gao, Zhigao Huang, Zhong Fang, Chen Fang, Hongming Weng, and Wei Zhang, “Evolution of weyl nodes in ni-doped thallium niobate pyrochlore $\text{tl}_2\text{-xnixnb}_2\text{o}_7$,” *Science China Physics, Mechanics & Astronomy* **65**, 297211 (2022).
- [26] Jiacheng Gao, Quansheng Wu, Clas Persson, and Zhijun Wang, “Irvsp: To obtain irreducible representations of electronic states in the vasp,” *Computer Physics Communications* **261**, 107760 (2021).
- [27] Jiacheng Gao, Zhaopeng Guo, Hongming Weng, and Zhijun Wang, “Magnetic band representations, fu-kane-like symmetry indicators, and magnetic topological materials,” *Phys. Rev. B* **106**, 035150 (2022).
- [28] Barry Bradlyn, L. Elcoro, Jennifer Cano, M. G. Vergniory, Zhijun Wang, C. Felser, M. I. Aroyo, and B. Andrei Bernevig, “Topological quantum chemistry,” *Nature* **547**, 298–305 (2017).
- [29] Hoi Chun Po, Ashvin Vishwanath, and Haruki Watanabe, “Symmetry-based indicators of band topology in the 230 space groups,” *Nature Communications* **8**, 50 (2017).
- [30] Haruki Watanabe, Hoi Chun Po, and Ashvin Vishwanath, “Structure and topology of band structures in the 1651 magnetic space groups,” *Science Advances* **4**, eaat8685 (2018).
- [31] Zhida Song, Tiantian Zhang, Zhong Fang, and Chen Fang, “Quantitative mappings between symmetry and topology in solids,” *Nature Communications* **9**, 3530 (2018).
- [32] Zhida Song, Tiantian Zhang, and Chen Fang, “Diagnosis for nonmagnetic topological semimetals in the absence of spin-orbital coupling,” *Phys. Rev. X* **8**, 031069 (2018).
- [33] Eslam Khalaf, Hoi Chun Po, Ashvin Vishwanath, and Haruki Watanabe, “Symmetry indicators and anomalous surface states of topological crystalline insulators,” *Phys. Rev. X* **8**, 031070 (2018).
- [34] Bingrui Peng, Yi Jiang, Zhong Fang, Hongming Weng, and Chen Fang, “Topological classification and diagnosis in magnetically ordered electronic materials,” *Phys. Rev. B* **105**, 235138 (2022).
- [35] Tiantian Zhang, Yi Jiang, Zhida Song, He Huang, Yuqing He, Zhong Fang, Hongming Weng, and Chen Fang, “Catalogue of topological electronic materials,” *Nature* **566**, 475–479 (2019).
- [36] Xiao Wang, Wen Li, Chen Wang, Juan Li, Xinyue Zhang, Bin-qiang Zhou, Yue Chen, and Yanzhong Pei, “Single parabolic band transport in p-type euzn_2sb_2 thermoelectrics,” *J. Mater. Chem. A* **5**, 24185–24192 (2017).
- [37] Jing Shuai, Jun Mao, Shaowei Song, Qinyong Zhang, Gang Chen, and Zhifeng Ren, “Recent progress and future challenges on thermoelectric zintl materials,” *Materials Today Physics* **1**, 74–95 (2017).
- [38] Chen Chen, Wenhua Xue, Shan Li, Zongwei Zhang, Xiaofang Li, Xinyu Wang, Yijie Liu, Jiehe Sui, Xingjun Liu, Feng Cao, Zhifeng Ren, Ching-Wu Chu, Yumei Wang, and Qian Zhang, “Zintl-phase $\text{eu}_2\text{zn}_2\text{sb}_2$: A promising thermoelectric material with ultralow thermal conductivity,” *Proceedings of the National Academy of Sciences* **116**, 2831–2836 (2019).
- [39] Damian Rybicki, Kamila Komędera, Janusz Przewoźnik, Łukasz Gondek, Czesław Kapusta, Karolina Podgórska, Wojciech Tabiś, Jan Żukrowski, Lan Maria Tran, Michał Babij, Zbigniew Bukowski, Ladislav Havela, Volodymyr Buturlim, Jiri Prchal, Martin Divis, Petr Kral, Ilja Turek, Itzhak Halevy, Jiri Kastil, Martin Misek, Utpal Dutta, and Dominik Legut, “Ambient- and high-pressure studies of structural, electronic, and magnetic properties of single-crystal euzn_2p_2 ,” *Phys. Rev. B* **110**, 014421 (2024).
- [40] Tanya Berry, Veronica J. Stewart, Benjamin W. Y. Redemann, Chris Lygouras, Nicodemos Varnava, David Vanderbilt, and Tyrel M. McQueen, “*a*-type antiferromagnetic order in the zintl-phase insulator euzn_2p_2 ,” *Phys. Rev. B* **106**, 054420 (2022).
- [41] Yuanfeng Xu, Zhida Song, Zhijun Wang, Hongming Weng, and Xi Dai, “Higher-order topology of the axion insulator euin_2as_2 ,” *Phys. Rev. Lett.* **122**, 256402 (2019).
- [42] Jingyu Yao, Ruihan Zhang, Sheng Zhang, Haohao Sheng, Youguo Shi, Zhong Fang, Hongming Weng, and Zhijun Wang, “Axion insulator, weyl points, quantum anomalous hall effect, and magnetic topological phase transition in $\text{eu}_3\text{in}_2\text{as}_4$,” *Phys. Rev. B* **111**, L041117 (2025).
- [43] Inga Schellenberg, Ulrike Pfannenschmidt, Matthias Eul, Christian Schwickert, and Rainer Pöttgen, “A 121sb and 151eu mössbauer spectroscopic investigation of eucd_2x_2 ($\text{x} = \text{p}, \text{as}, \text{sb}$) and ybcd_2sb_2 ,” *Zeitschrift für anorganische und allgemeine Chemie* **637**, 1863–1870 (2011).
- [44] Jyoti Krishna, T. Nautiyal, and T. Maitra, “First-principles study of electronic structure, transport, and optical properties of eucd_2as_2 ,” *Phys. Rev. B* **98**, 125110 (2018).
- [45] J.-Z. Ma, S. M. Nie, C. J. Yi, J. Jandke, T. Shang, M. Y. Yao, M. Naamneh, L. Q. Yan, Y. Sun, A. Chikina, V. N. Strocov, M. Medarde, M. Song, Y.-M. Xiong, G. Xu, W. Wulfhekkel, J. Mesot, M. Reticioli, C. Franchini, C. Mudry, M. Müller, Y. G. Shi, T. Qian, H. Ding, and M. Shi, “Spin fluctuation induced weyl semimetal state in the paramagnetic phase of eucd_2as_2 ,” *Science Advances* **5**, eaaw4718 (2019).
- [46] M. C. Rahn, J.-R. Soh, S. Francoual, L. S. I. Veiga, J. Stempffer, J. Mardegan, D. Y. Yan, Y. F. Guo, Y. G. Shi, and A. T. Boothroyd, “Coupling of magnetic order and charge transport in the candidate dirac semimetal eucd_2as_2 ,” *Phys. Rev. B* **97**, 214422 (2018).
- [47] J.-R. Soh, F. de Juan, M. G. Vergniory, N. B. M. Schröter, M. C. Rahn, D. Y. Yan, J. Jiang, M. Bristow, P. Reiss, J. N. Blandy, Y. F. Guo, Y. G. Shi, T. K. Kim, A. McCollam, S. H. Simon, Y. Chen, A. I. Coldea, and A. T. Boothroyd, “Ideal weyl semimetal induced by magnetic exchange,” *Phys. Rev. B* **100**, 201102 (2019).
- [48] Lin-Lin Wang, Na Hyun Jo, Brinda Kuthanazhi, Yun Wu, Robert J. McQueeney, Adam Kaminski, and Paul C. Canfield, “Single pair of weyl fermions in the half-metallic semimetal EuCd_2As_2 ,” *Phys. Rev. B* **99**, 245147 (2019).
- [49] H. P. Wang, D. S. Wu, Y. G. Shi, and N. L. Wang, “Anisotropic transport and optical spectroscopy study on antiferromagnetic triangular lattice eucd_2as_2 : An interplay between magnetism and charge transport properties,” *Phys. Rev. B* **94**, 045112 (2016).

- [50] Yu Goryunov, V Fritsch, H v Löhneysen, and A Nateprov, “The esr study of eu ternary pnictides euCd_2Sb_2 , euZn_2As_2 ,” *Journal of Physics: Conference Series* **391**, 012015 (2012).
- [51] Na Hyun Jo, Brinda Kuthanazhi, Yun Wu, Erik Timmons, Tae-Hoon Kim, Lin Zhou, Lin-Lin Wang, Benjamin G. Ueland, Andriy Palasyuk, Dominic H. Ryan, Robert J. McQueeney, Kyungchan Lee, Benjamin Schruck, Anton A. Burkov, Ruslan Prozorov, Sergey L. Bud’ko, Adam Kaminski, and Paul C. Canfield, “Manipulating magnetism in the topological semimetal euCd_2As_2 ,” *Phys. Rev. B* **101**, 140402 (2020).
- [52] Chengwang Niu, Ning Mao, Xiangting Hu, Baibiao Huang, and Ying Dai, “Quantum anomalous hall effect and gate-controllable topological phase transition in layered euCd_2As_2 ,” *Phys. Rev. B* **99**, 235119 (2019).
- [53] Azizur Rahman, Majeed Ur Rehman, Yue Zhang, Weisheng Zhao, Jianlin Wang, Zheng Chen, Zahir Muhammad, and Lei Zhang, “Exploring the tricritical nature and unconventional magnetoresistance in euCd_2P_2 : An in-depth study of complex material characteristics,” *Phys. Rev. B* **110**, 064407 (2024).
- [54] Zhi-Cheng Wang, Jared D. Rogers, Xiaohan Yao, Renee Nichols, Kemal Atay, Bochao Xu, Jacob Franklin, Ilya Sochnikov, Philip J. Ryan, Daniel Haskel, and Fazel Tafti, “Colossal magnetoresistance without mixed valence in a layered phosphide crystal,” *Advanced Materials* **33**, 2005755 (2021).
- [55] Huali Zhang, Feng Du, Xiaoying Zheng, Shuaishuai Luo, Yi Wu, Hao Zheng, Shengtao Cui, Zhe Sun, Zhengtai Liu, Dawei Shen, Michael Smidman, Yu Song, Ming Shi, Zhicheng Zhong, Chao Cao, Huiqiu Yuan, and Yang Liu, “Electronic band reconstruction across the insulator-metal transition in colossally magnetoresistive euCd_2P_2 ,” *Phys. Rev. B* **108**, L241115 (2023).
- [56] Mizuki Ohno, Susumu Minami, Yusuke Nakazawa, Shin Sato, Markus Kriener, Ryotaro Arita, Masashi Kawasaki, and Masaki Uchida, “Maximizing intrinsic anomalous hall effect by controlling the fermi level in simple weyl semimetal films,” *Phys. Rev. B* **105**, L201101 (2022).
- [57] Y. Takagiwa, Y. Sato, A. Zevalkink, I. Kanazawa, K. Kimura, Y. Isoda, and Y. Shinohara, “Thermoelectric properties of euZn_2Sb_2 zintl compounds: zt enhancement through yb substitution for eu,” *Journal of Alloys and Compounds* **703**, 73–79 (2017).
- [58] W. Kohn and L. J. Sham, “Self-consistent equations including exchange and correlation effects,” *Phys. Rev.* **140**, A1133–A1138 (1965).
- [59] G. Kresse and J. Furthmüller, “Efficient iterative schemes for ab initio total-energy calculations using a plane-wave basis set,” *Phys. Rev. B* **54**, 11169–11186 (1996).
- [60] P. E. Blöchl, “Projector augmented-wave method,” *Phys. Rev. B* **50**, 17953–17979 (1994).
- [61] John P. Perdew, Kieron Burke, and Matthias Ernzerhof, “Generalized gradient approximation made simple,” *Phys. Rev. Lett.* **77**, 3865–3868 (1996).
- [62] John P. Perdew, Kieron Burke, and Matthias Ernzerhof, “Generalized gradient approximation made simple [phys. rev. lett. 77, 3865 (1996)],” *Phys. Rev. Lett.* **78**, 1396–1396 (1997).
- [63] S. L. Dudarev, G. A. Botton, S. Y. Savrasov, C. J. Humphreys, and A. P. Sutton, “Electron-energy-loss spectra and the structural stability of nickel oxide: An lsd+u study,” *Phys. Rev. B* **57**, 1505–1509 (1998).
- [64] Hendrik J. Monkhorst and James D. Pack, “Special points for brillouin-zone integrations,” *Phys. Rev. B* **13**, 5188–5192 (1976).
- [65] Arash A. Mostofi, Jonathan R. Yates, Giovanni Pizzi, Young-Su Lee, Ivo Souza, David Vanderbilt, and Nicola Marzari, “An updated version of wannier90: A tool for obtaining maximally-localised wannier functions,” *Computer Physics Communications* **185**, 2309–2310 (2014).
- [66] Nafise Rezaei, Mojtaba Alaei, and Hadi Akbarzadeh, “Espins: A program for classical monte-carlo simulations of spin systems,” *Computational Materials Science* **202**, 110947 (2022).
- [67] QuanSheng Wu, ShengNan Zhang, Hai-Feng Song, Matthias Troyer, and Alexey A. Soluyanov, “Wanniertools: An open-source software package for novel topological materials,” *Computer Physics Communications* **224**, 405–416 (2018).
- [68] Greeshma C. Jose, Kaleb Burrage, Jose L. Gonzalez Jimenez, Weiwei Xie, Barbara Lavina, Jiyong Zhao, Esen E. Alp, Dongzhou Zhang, Yuming Xiao, Yogesh K. Vohra, and Wenli Bi, “Evolution of magnetism, valence, and crystal lattice in euCd_2As_2 under pressure,” *Phys. Rev. B* **107**, 245121 (2023).
- [69] Yi Jiang, Ziyin Song, Tiannian Zhu, Zhong Fang, Hongming Weng, Zheng-Xin Liu, Jian Yang, and Chen Fang, “Enumeration of spin-space groups: Toward a complete description of symmetries of magnetic orders,” *Phys. Rev. X* **14**, 031039 (2024).
- [70] Ziyin Song, A. Z. Yang, Yi Jiang, Zhong Fang, Jian Yang, Chen Fang, Hongming Weng, and Zheng-Xin Liu, “Constructions and applications of irreducible representations of spin-space groups,” (2024), arXiv:2409.13601 [cond-mat.mtrl-sci].
- [71] J.-R. Soh, C. Donnerer, K. M. Hughes, E. Schierle, E. Weschke, D. Prabhakaran, and A. T. Boothroyd, “Magnetic and electronic structure of the layered rare-earth pnictide euCd_2Sb_2 ,” *Phys. Rev. B* **98**, 064419 (2018).
- [72] Bingyang Li, Wenli Sun, Xiaorong Zou, Xinying Li, Baibiao Huang, Ying Dai, and Chengwang Niu, “Switchable quantum anomalous and spin hall effects in honeycomb magnet euCd_2As_2 ,” *New Journal of Physics* **24**, 053038 (2022).
- [73] Mizuki Ohno, Susumu Minami, Yusuke Nakazawa, Shin Sato, Markus Kriener, Ryotaro Arita, Masashi Kawasaki, and Masaki Uchida, “Maximizing intrinsic anomalous hall effect by controlling the fermi level in simple weyl semimetal films,” *Phys. Rev. B* **105**, L201101 (2022).
- [74] Zhiyu Liao, Boxuan Li, Shaohui Yi, Lincong Zheng, Yubiao Wu, Enkui Yi, Premysl Marsik, Bing Shen, Hongming Weng, Bing Xu, Xianggang Qiu, and Christian Bernhard, “Spectroscopic signatures of magnetization-induced band renormalization and strong spin-charge-lattice coupling in euZn_2As_2 ,” (2024), arXiv:2412.12728 [cond-mat.mtrl-sci].
- [75] Joanna Blawat, Madalynn Marshall, John Singleton, Erxi Feng, Huibo Cao, Weiwei Xie, and Rongying Jin, “Unusual electrical and magnetic properties in layered euZn_2As_2 ,” *Advanced Quantum Technologies* **5**, 2200012 (2022).
- [76] Tanya Berry, Veronica J. Stewart, Benjamin W. Y. Redemann, Chris Lygouras, Nicodemos Varnava, David Vanderbilt, and Tyrel M. McQueen, “*a*-type antiferromagnetic order in the zintl-phase insulator euZn_2P_2 ,” *Phys. Rev. B* **106**, 054420 (2022).
- [77] Xiyu Chen, Wuzhang Yang, Jia-Yi Lu, Zhiyu Zhou, Zhi Ren, Guang-Han Cao, Shuai Dong, and Zhi-Cheng Wang, “Carrier-induced transition from antiferromagnetic insulator to ferromagnetic metal in the layered phosphide euZn_2P_2 ,” *Phys. Rev. B* **109**, L180410 (2024).
- [78] Zhi-Cheng Wang, Emily Been, Jonathan Gaudet, Gadeer Matook A. Alqasseri, Kyle Fruhling, Xiaohan Yao, Uwe Stuhr, Qinqing Zhu, Zhi Ren, Yi Cui, Chunjing Jia, Brian Moritz, Sugata Chowdhury, Thomas Devereaux, and Fazel Tafti, “Anisotropy of the magnetic and transport properties of

- euzn₂as₂,” *Phys. Rev. B* **105**, 165122 (2022).
- [79] Sarah Krebber, Marvin Kopp, Charu Garg, Kurt Kummer, Jörg Sichelschmidt, Susanne Schulz, Georg Poelchen, Max Mende, Alexander V. Virovets, Konstantin Warawa, Mark D. Thomson, Artem V. Tarasov, Dmitry Yu. Usachov, Denis V. Vylikh, Hartmut G. Roskos, Jens Müller, Cornelius Krellner, and Kristin Kliemt, “Colossal magnetoresistance in euzn₂p₂ and its electronic and magnetic structure,” *Phys. Rev. B* **108**, 045116 (2023).
- [80] Karan Singh, Shovan Dan, A. Ptok, T. A. Zaleski, O. Pavlosiuk, P. Wiśniewski, and D. Kaczorowski, “Superexchange interaction in insulating euzn₂p₂,” *Phys. Rev. B* **108**, 054402 (2023).
- [81] J.-R. Soh, C. Donnerer, K. M. Hughes, E. Schierle, E. Weschke, D. Prabhakaran, and A. T. Boothroyd, “Magnetic and electronic structure of the layered rare-earth pnictide eucd₂sb₂,” *Phys. Rev. B* **98**, 064419 (2018).
- [82] Eliot Heinrich, Ayano Nakamura, Shinichi Nishihaya, Eugen Weschke, Henrik Rønnow, Masaki Uchida, Benedetta Flebus, and Jian-Rui Soh, “Magnetic structure of a single-crystal thin film of eucd₂sb₂,” *Phys. Rev. B* **110**, 024405 (2024).
- [83] Peter Klüfers, Hermann Neumann, Albrecht Mewis, and Hans-Uwe Schuster, “Ab₂x₂-verbindungen im caal₂si₂-typ, viii [1] / ab₂x₂ compounds with the caal₂si₂ structure, viii [1],” *Zeitschrift für Naturforschung B* **35**, 1317–1318 (1980).
- [84] Joanna Blawat, Madalynn Marshall, John Singleton, Erxi Feng, Huibo Cao, Weiwei Xie, and Rongying Jin, “Unusual electrical and magnetic properties in layered euzn₂as₂,” *Advanced Quantum Technologies* **5**, 2200012 (2022).
- [85] Andrew F. May, Michael A. McGuire, Jie Ma, Olivier Delaire, Ashfia Huq, and Radu Custelcean, “Properties of single crystalline azn₂sb₂ (a = ca,eu,yb),” *Journal of Applied Physics* **111**, 033708 (2012).
- [86] A. Artmann, A. Mewis, M. Roepke, and G. Michels, “Am₂x₂-verbindungen mit caal₂si₂-struktur. xi. struktur und eigenschaften der verbindungen acd₂x₂ (a: Eu, yb; x: P, as, sb),” *Zeitschrift für anorganische und allgemeine Chemie* **622**, 679–682 (1996).
- [87] Zhi-Cheng Wang, Jared D. Rogers, Xiaohan Yao, Renee Nichols, Kemal Atay, Bochao Xu, Jacob Franklin, Ilya Sochnikov, Philip J. Ryan, Daniel Haskel, and Fazel Tafti, “Colossal magnetoresistance without mixed valence in a layered phosphide crystal,” *Advanced Materials* **33**, 2005755 (2021).
- [88] Hao Su, Benchao Gong, Wujun Shi, Haifeng Yang, Hongyuan Wang, Wei Xia, Zhenhai Yu, Peng-Jie Guo, Jinhua Wang, Linchao Ding, Liangcai Xu, Xiaokang Li, Xia Wang, Zhiqiang Zou, Na Yu, Zengwei Zhu, Yulin Chen, Zhongkai Liu, Kai Liu, Gang Li, and Yanfeng Guo, “Magnetic exchange induced weyl state in a semimetal eucd₂sb₂,” *APL Materials* **8**, 011109 (2020).
- [89] Inga Schellenberg, Matthias Eul, Wilfried Hermes, and Rainer Pöttgen, “A 121sb and 151eu mössbauer spectroscopic investigation of eumn₂sb₂, euzn₂sb₂, ybmn₂sb₂, and ybzn₂sb₂,” *Zeitschrift für anorganische und allgemeine Chemie* **636**, 85–93 (2010).
- [90] H. J. Xiang, E. J. Kan, Su-Huai Wei, M.-H. Whangbo, and X. G. Gong, “Predicting the spin-lattice order of frustrated systems from first principles,” *Phys. Rev. B* **84**, 224429 (2011).
- [91] Hongjun Xiang, Changhoon Lee, Hyun-Joo Koo, Xingao Gong, and Myung-Hwan Whangbo, “Magnetic properties and energy-mapping analysis,” *Dalton Trans.* **42**, 823–853 (2013).
-

Supplemental Material 'Manipulation of topological phase transitions and the mechanism of magnetic interactions in Eu-based Zintl-phase materials'

Bo-Xuan Li^{1,2}, Ziyin Song^{1,2}, Zhong Fang^{1,2}, Zhijun Wang^{1,2}, Hongming Weng^{1,2,3,*}

¹Beijing National Laboratory for Condensed Matter Physics and Institute of Physics, Chinese Academy of Sciences, Beijing 100190, China

²University of Chinese Academy of Sciences, Beijing 100049, China

³Songshan Lake Materials Laboratory, Dongguan 523808, China

This supplemental material contains the orbit projections of EuCd_2As_2 with AFM-Aa magnetic configuration FIG.S1 and the comparison between calculated optical conductivity and experimental transmission results of EuZn_2As_2 with the AFM-Aa magnetic configuration FIG.S2.

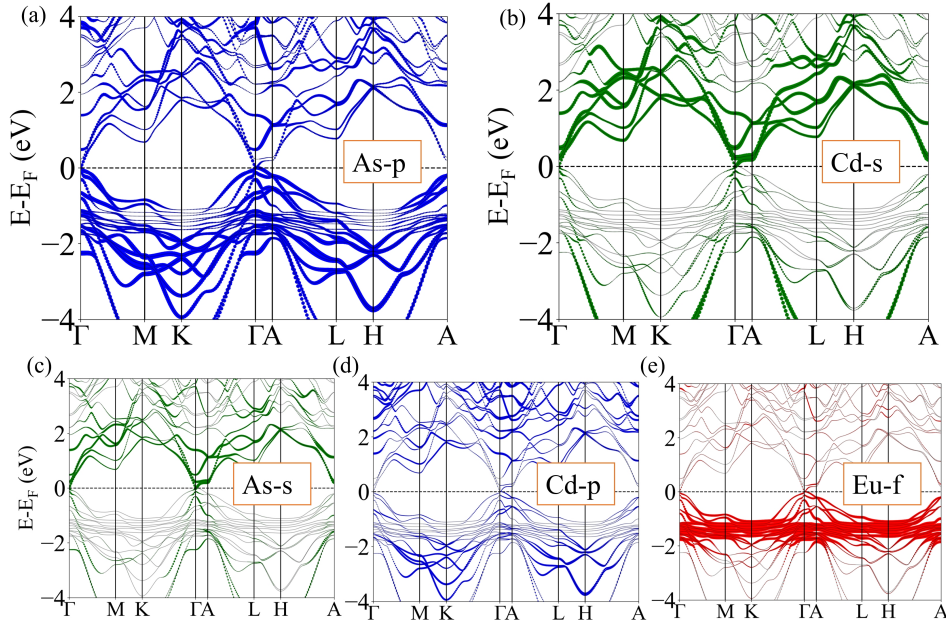


FIG. S1. (a)-(e) show different orbit projections of EuCd_2As_2 with AFM-Aa magnetic configuration

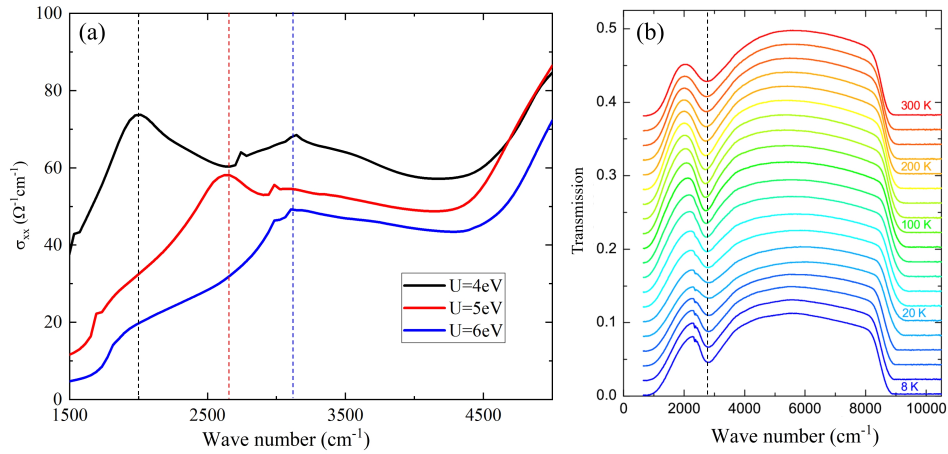


FIG. S2. (a) Calculated optical conductivity of EuZn_2As_2 with the AFM-Aa magnetic configuration for various Hubbard- U values. The dotted lines indicate the peak around the wave number of 3000 cm^{-1} . (b) Transmission results of EuZn_2As_2 with the AFM-Aa magnetic configuration as a function of peak wave number at different temperatures.